THE JOURNAL OF PHYSICAL CHEMISTRY C
A JOURNAL OF THE AMERICAN CHEMICAL SOCIETY

Open Access

pubs.acs.org/JPCC

Article

Iron–Water Interface at Different Electrochemical Conditions

Published as part of The Journal of Physical Chemistry C special issue "Francesc Illas and Gianfranco Pacchioni Festschrift".

Adenilson Felipe Sousa-Silva, Dídac-Armand Fenoll, Mariona Sodupe, Luis Rodríguez-Santiago,* and Xavier Solans-Monfort*

Cite This: *J. Phys. Chem. C* 2025, 129, 18666–18675

Read Online

ACCESS | Metrics & More | Article Recommendations | Supporting Information

ABSTRACT: Understanding the interaction between water and electrocatalyst surfaces, as well as the structure of the interface at different applied potentials, is of great importance for improving the efficiency of electrochemical processes, such as hydrogen evolution, CO_2 reduction, and nitrogen fixation. In this study, density functional theory (DFT) simulations are employed to explore the interaction of water with different crystalline facets of body-centered cubic iron—namely, Fe(100), Fe(110), and Fe(111)—under different electrochemical conditions. For that, we considered several water coverages, from an isolated molecule to a full monolayer. Simulations reveal that at low coverages, water dissociates twice, forming *O and 2 *H on the three surfaces. However, increasing coverage reduces the availability of favorable adsorption sites, lowering the energy benefits of dissociation. The hydrogen bonding between adsorbed and nonadsorbed water molecules does not depend on water coverage; thus, for the full H_2O monolayer, the preferred structure involves 50% dissociation for the three facets, normally without the presence of *O species on the surface. Results also show that each facet responds differently to the applied potential. According to the computed Pourbaix diagrams, under reducing potentials typical of N_2 or CO_2 electroreduction, Fe(110) and Fe(111) are covered with a full hydrogen monolayer, while Fe(100) presents a lower H-coverage at the usual cathodic potentials.

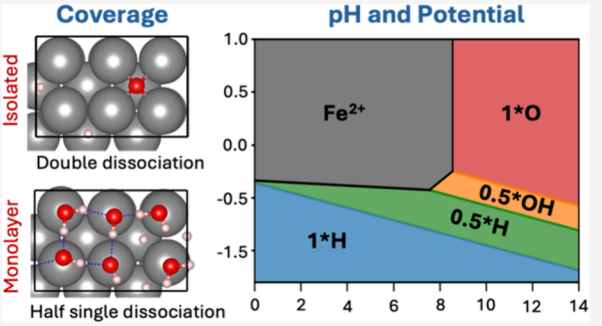

INTRODUCTION

Electrocatalysis in water-based electrolytes is seen as a promising alternative to the fossil-fuel-based chemical industry. Electrocatalysis has been used for sunlight energy storage in the H–H chemical bond of H_2 through water electrolysis, the green synthesis of organic compounds through CO_2 reduction, and fertilizer synthesis through N_2 and NO_3^- reduction. In all these processes, understanding how water interacts with the electrode interface, including the interplay between metal surfaces and water molecules, is crucial for characterizing the active site's electronic structure under reaction conditions.[1] Furthermore, the oxidation state of the electrocatalysts' surfaces can change through water mediation or even directly, depending on their tendency to dissociate on those metal surfaces. Through its dissociation, water becomes a source of *H, *OH, and *O moieties, which are key intermediates in several redox processes, including the hydrogen evolution reaction (HER) and the oxygen evolution reaction (OER). Given its low overpotential even in alkaline media, the HER is competitive with any process requiring highly reductive potentials, ultimately lowering its faradaic efficiencies.

Currently, most electrocatalysts achieving the highest current densities combined with significant stabilities are based on costly noble metal electrodes. These include Pt as the gold standard for the HER and IrO_X as the reference catalyst for the OER at acidic conditions. Process up-scaling, however, requires reducing the dependence on noble metals, which has drawn attention to Earth-abundant alternatives such as Cu or Fe.[2,3] In this regard, iron oxides and iron oxyhydroxides have attracted significant attention for several electrocatalytic processes owing to their abundance and low toxicity.[4−9] Moreover, while Fe-based materials are far from ideal HER electrocatalysts,[10] they are interesting candidates for other reduction reactions such as CO_2 reduction (CO_2RR) or N_2 reduction (N_2RR).[11] Indeed, aside from their ubiquitous presence in industrial infrastructure,[12] Fe-based materials have a distinct role in the synthesis of ammonia through the Haber–Bosch process, prompting their use in the N_2RR as a source of

Received: June 16, 2025
Revised: August 29, 2025
Accepted: September 12, 2025
Published: October 1, 2025

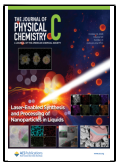

green ammonia. However, the reported iron electrocatalysts do not achieve satisfactory faradaic efficiencies to balance out upscaling costs.[11]

Water adsorption on low-index (100), (110), and (111) facets of α-iron (body-centered cubic, bcc) has been characterized through various spectroscopic techniques. Auger electron spectroscopy (AES), electron energy loss spectroscopy (EELS), and low-energy electron diffraction (LEED) suggest that water chemisorption on both Fe(100) and Fe(110) surfaces through H_2O dissociation is preferred over molecular physisorption.[13−15] However, at low temperatures, physisorption is more frequently observed, which points to the existence of a non-negligible energy barrier for water dissociation.

Additionally, there is a limited number of first-principles studies focusing on the atomistic insights of H_2O adsorption on iron.[16−23] Most of the contributions are centered on the most stable Fe(100) and Fe(110) surfaces, for which the effect of water coverage on the H_2O adsorption energy and dissociation is limited to a single surface. Results show that dissociation of water to either *OH + *H or *O + *2H is thermodynamically favorable. However, while the energy barrier for *OH/*H formation is reported to be accessible and facilitated by increasing the number of explicitly added water molecules, the formation of *O requires overcoming significantly higher energy barriers. Moreover, H_2O adsorption on stepped facets is predicted to be stronger, therefore facilitating water dissociation on these sites.

Remarkably, in the previously mentioned contributions, the effect of an applied potential was not considered. Only recently, Kavalsky and Viswanathan explored the water Fe(110) interface at different applied potentials,[24] reporting that at cathodic potentials, Fe(110) presents a monolayer of *H atoms and at potentials around −0.2 V the favored process implies Fe dissolution. To the best of our knowledge, there is not a systematic study analyzing the effect of water coverage and applied potential on the structure of the water−iron interface for multiple iron surfaces, that is, factoring in the role of surface morphology.

In this contribution, we examine the interaction between interfacial water molecules and three low-index *bcc* Fe facets at the density functional theory (DFT) level. Attention is drawn to the effect of surface coverage and mediation of hydrogen bonding on the dissociation of water at the most stable sites. Both pristine and fully reduced/oxidized surfaces are considered with the ultimate goal of reproducing a wide range of operando conditions. Calculations show that water dissociation on Fe surfaces occurs on all the facets. The extent of the dissociation, however, depends on water surface coverage and surface morphology. Pourbaix diagrams of the three surfaces show that on (110) and (111), formation of one *H monolayer occurs at low reducing potentials, while on (100) *H monolayer formation requires stronger cathodic potentials. Consequently, simulations suggest that under the most common conditions for N_2, NO_3^-, and CO_2 electrocatalytic reduction reactions, Fe surfaces are likely covered either by a *H half monolayer (100) or by a full *H monolayer ((110) and (111)).

COMPUTATIONAL DETAILS

Periodic simulations are performed using the VASP code.[25,26] This software imposes periodicity in the three dimensions; thus, at least 18 Å of vacuum space between images along the nonperiodic direction was enforced to minimize spurious interactions.

Models. Three surface slab models are considered [(100), (110), and (111)] (see Figure 1). The (100) and (110) are the most stable facets, while the (111) is considered to analyze the effect of surface roughness. The models are constructed by cutting the iron *bcc* bulk with ASE (Atomic Simulation Environment)[27] and expanding the unit cell to a (2 × 3) for (100) and (2 × 2) for (110) and (111) supercell to allow larger flexibility for the adsorbed water molecules. Slab thickness was set to 6 layers for (100) and (110) and 4 layers for (111), based on a previous calibration study.

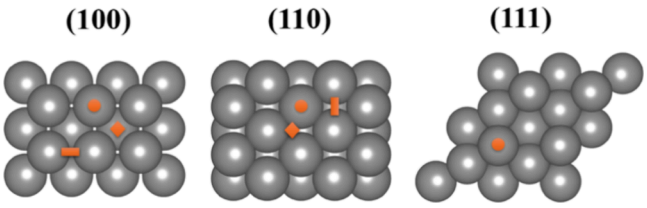

Figure 1. Apical view of the optimized Fe surface slab models herein considered. In orange: top (circle), bridge (rectangle), and hollow sites (rhombus).

Level of Theory. Simulations at the DFT level were carried out using the GGA PBE[28] exchange-correlation functional. Dispersion corrections were introduced through Grimme's D3 parametrization.[29] Magnetization is known to be present in all of the explored systems, for which spin-polarization was enforced by applying μ = 2.3 μ_B on all iron centers. Atomic cores were represented with projector augmented wave (PAW) pseudopotentials.[30,31] Geometry optimizations were performed imposing a kinetic energy cutoff of 600 eV and a 6×6×1 Monkhorst−Pack *k*-point grid for the supercells, except for the case of the most computationally demanding (111) surface. For this surface, the kinetic energy cutoff was set to 400 eV and the Monkhorst−Pack *k*-point grid to 4×4×1. Benchmark calculations demonstrated that this selection converged surface energies to 1 meV/Å^2 with respect to the *k*-point grids and the adsorption energy of one water molecule to 30 meV with respect to the energy cutoff. The ionic relaxation threshold was set to 0.01 eV/Å, ensuring that the norms of all forces are converged within this threshold. Moreover, the effect of the rest of the electrolyte was taken into account using the implicit water solvation model implemented in VASPsol[32] through single-point calculations. Atomic charges were calculated through Bader charge analysis.[33,34]

Thermal effects were evaluated at 1 atm and 298 K following the approximation proposed by Nørskov et al.;[35] thus, Gibbs energies are calculated as follows:

$$G \approx E_{DFT} + E_{ZPE} - T \cdot S_{vib}$$

The E_{ZPE} and S_{vib} terms are neglected for bulk and pristine surfaces. For the water−surface structures, these terms are obtained from the vibrational modes of the adsorbed water molecules and assuming the harmonic oscillator approximation, as implemented in VASPkit.[36] For that, we fixed the positions of all iron atoms and performed finite displacements of 0.02 Å in each direction for all species of the adsorbed H_2O. Conventionally, vibrational frequencies below 50 cm^{-1} are rounded up to this value to avoid spurious entropy contributions from low-frequency modes. The entropy terms

https://doi.org/10.1021/acs.jpcc.5c04170
J. Phys. Chem. C 2025, 129, 18666−18675

of H_2O and H_2 were taken from tabulated values for liquid H_2O and gas-phase H_2, respectively. This strategy is analogous to some of our previous contributions on H_2O−surface interactions.[37−39]

Surface Gibbs energies of the pristine facets are calculated as follows:

$$\gamma_{ijk} = \frac{E_{slab} - N \cdot E_{bulk}}{2A}$$

That is, the potential energy difference between the surface slab (E_{slab}) and the bulk (E_{bulk}) material per unit area (A), adjusted to the number of surface atoms compared to the bulk (N). Note that the surface area must be doubled because there are two slab-vacuum interfaces in the periodic model.

Adsorption energies (ΔE_{ads}) and Gibbs adsorption energies (ΔG_{ads}) of water molecules were computed as follows:

$$\Delta E_{ads} = \frac{1}{n}(E_{slab-nH_2O} - E_{slab} - nE_{H_2O})$$

$$\Delta G_{ads} = \frac{1}{n}(G_{slab-nH_2O} - E_{slab} - nG_{H_2O})$$

where n is the number of water molecules adsorbed and $G_{slab-nH_2O}$, E_{slab}, and G_{H_2O} are the Gibbs energies of the water−surface structure, pristine surface, and an isolated water molecule, respectively.

Surface changes may occur after each proton-coupled electron transfer (PCET) step. The reactions connecting the different states of the surface can be written as:

$$^*H_{x-n}O_y + nH^+ + ne^- \rightarrow {}^*H_xO_y$$

The ΔG^0 for these PCET steps are computed by using the computational hydrogen electrode as defined by Rossmeisl, Nørskov and co-workers, which estimates the Gibbs energy of the proton and an electron with half a hydrogen molecule versus the reversible hydrogen electrode, or equivalently, the standard hydrogen electrode (SHE) at pH = 0.[35] In this approximation, the effect of the applied potential is included by shifting the energy of each step by $-eU$, where U is the electrode potential. At a pH different from 0, the free energy of the H^+ ions versus SHE can be obtained by considering the H^+ activity dependence: ΔG_{pH} (pH) = $- k_B T \ln a_{H+}$. Overall, the reaction free energy of n consecutive PCET processes at a given applied potential U referenced to the SHE is calculated as follows:

$$\Delta G(U, pH) = G_{^*H_xO_y} - G_{^*H_{x-n}O_y} - \frac{n}{2}G_{H_2} + k_B T \ln a_{H^+} + neU$$

The values obtained using this protocol allow us to predict the most thermodynamically stable surface phases as a function of the applied potential, U, and pH, in a representation known as a Pourbaix diagram.

In addition to the surface phases, we also consider the iron dissolution reaction:

$$Fe_{(s)} \rightarrow Fe^{2+}_{(aq)} + 2e^-$$

the energy change for Fe dissolution at $a_{Fe^{2+}} = 1$ can be obtained as follows:

$$\Delta G_{diss} = -2e(U - E_{Fe^{2+}/Fe})$$

where $E_{Fe^{2+}/Fe}$ is the redox potential of iron at standard conditions (−0.45 V vs SHE).[40] It is worth noting that this is independent of the pH.

RESULTS AND DISCUSSION

Results are divided into five sections. First, we discuss the characterization of the three pristine Fe facets. Next, we focus on the adsorption of an isolated water molecule, in either molecular or dissociated forms. In the third section, we focus on the adsorption of two water molecules, and in the fourth section, we focus on the formation of one water monolayer. Finally, the stability of different surface terminations at varying applied potentials and pH is discussed by means of Pourbaix diagrams.

Pristine Surfaces. Selected data for the pristine (100), (110), and (111) surfaces are presented in Table 1. The computed surface energies show that the three facets have similar surface energies, although the (110) and (100) surfaces are flat and the (111) surface is distinctively rough. Despite their flatness, (100) and (110) present different surface Fe−Fe and interlayer distances, pointing at different surface morphologies and dissimilar surface metal coordination environments. Indeed, top sites on (110) are almost 0.4 Å closer than those in the (100) surface, and metal centers appear to interact more strongly with other Fe centers of the material. Moreover, as shown in Figure 1, while the (100) surface presents hollow sites with a coordination number of 5 and bridge sites, the (110) surface also presents bridge sites and locations where the adsorbed species interacts with three surface atoms (henceforth referred to as 3-fold hollow sites). For (111), the surface presents at least three layers capable of interfacing with adsorbed species. These layers are near each other with an interlayer distance of only 0.839 Å for the two outermost layers.

Table 1. Surface Gibbs Energy (γ_{ijk}) and Area (A), Surface Iron−Iron ($d_{Fe\cdots Fe}$) and Fe−Fe Interlayer (δ_{12}) Distances, and Bader Charges of the Outermost Fe Centers (Q)[a]

	(100)	(110)	(111)
γ_{ijk}	0.198	0.193	0.199
A	47.2	44.5	54.4
$d_{Fe\cdots Fe}$	2.803	2.428	3.965
δ_{12}	1.426	2.000	0.839
Q	+0.08	−0.01	+0.17/−0.16

[a]All energy units are in eV; length and area units are in Å and Å^2, and charges in e. Surface Gibbs energies are given in eV/Å^2.

Another difference between (110), (100), and (111) surfaces is the Bader charges on the outermost Fe ions. Charges on the Fe centers for (100) and (110) are close to zero and are uniformly distributed. In contrast, the two outermost Fe layers of the (111) surface present charges of opposite sign, with most external atoms being positively charged. This is correlated to a change in the Fe oxidation state, which increases for Fe in the most external layer as inferred from the magnetic moments (Figure 2).

Adsorption of an Isolated Water Molecule. Before analyzing all molecular and dissociated forms of water on the three surfaces, we first exhaustively explored the adsorption of the 4 possible resulting species ($^*H_2O$, *OH, *O, and *H) adsorbed on the different sites of the three surfaces (top, bridge, asymmetric bridges, 3-fold, and hollow). Results for

https://doi.org/10.1021/acs.jpcc.5c04170
J. Phys. Chem. C 2025, 129, 18666−18675

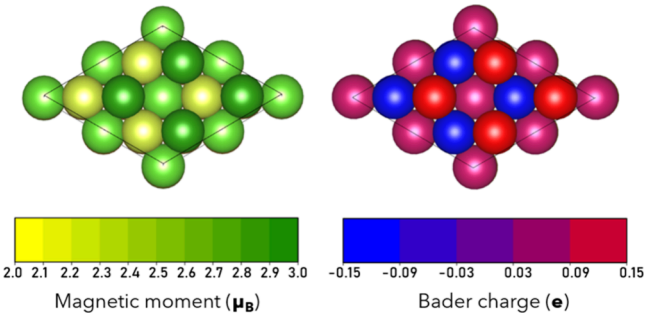

Figure 2. Color-graded magnetic moments and Bader charges of the outermost Fe atoms on Fe (111).

*OH, *O, and *H are summarized in Figures S1−S3. H_2O prefers to adsorb on the top site, regardless of the surface, and it is discussed below. The *OH is preferentially adsorbed on (100) bridge sites, (110) 3-fold sites, and (111) asymmetric bridge sites, respectively. Finally, the atomic *H and *O species prefer to be on the most coordinated (100) hollow, (110) 3-fold, and (111) asymmetric bridge sites.

From these data, the initial structures for molecular, mono-, and bis-dissociated forms were constructed considering the most stable site of each fragment on each surface. Moreover, we also considered other possibilities to ensure the absence of interactions between the fragments. The lowest in energy computed structures obtained are shown in Figure 3.

For the three surfaces, molecular water adsorbs on the top positions, adopting a parallel conformation with respect to the surface. This adsorption mode has been shown to be the preferred one in previous contributions.[16−23] The Fe···O distances are 2.21 Å for the (100) and (110) surfaces and 2.13 Å for the (111) one. However, this structural difference is not reflected in the Gibbs adsorption energies, which are all similarly weak, ranging from −0.32 to −0.37 eV. The interaction between the surface and the adsorbed water molecule is mainly driven by dispersion and electrostatics, as evidenced by Bader charge analysis, which indicates minimal ligand-surface charge transfer (Figure S4).

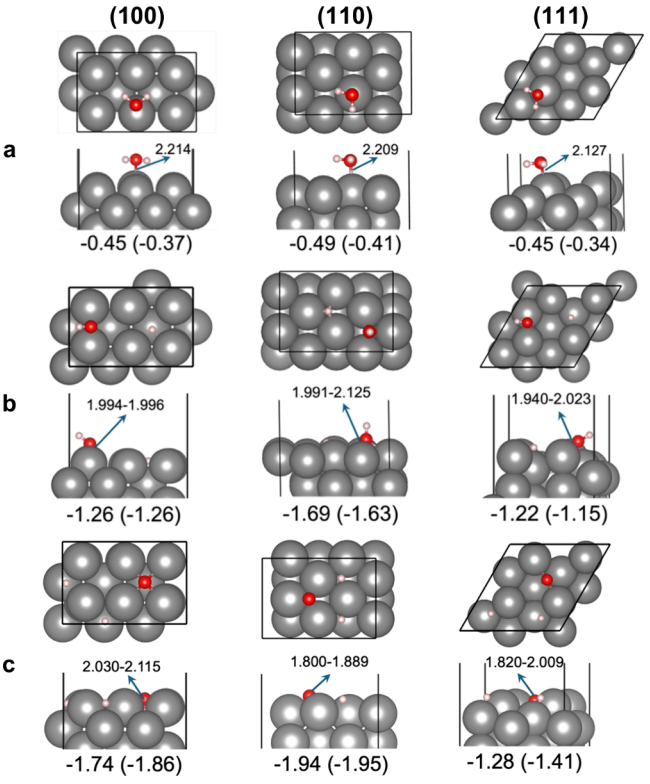

Figure 3. Top and side views of an adsorbed water in its molecular (a), monodissociated (b), and bis-dissociated (c) forms. Adsorption energies (Gibbs adsorption energies in parentheses) in eV and O···Fe distances in Å.

Adsorption of a dissociated water molecule takes place at different sites depending on the surface, in agreement with previous studies.[16−19,21−23] For the (100) facet, the most stable configuration involves *OH adsorbed on a bridge site and *H in the hollow. For Fe(110), both species, *H and *OH, adsorb on a 3-fold hollow site. Finally, on Fe(111), the adsorption occurs with *OH and *H interacting with Fe atoms of the two outermost layers in locations that resemble an asymmetric bridge site. As expected, Fe···O distances are shorter than those of the molecular adsorbed form in the three surfaces, with the average values ranging from 1.99 to 2.13 Å.

Water dissociation on the Fe facets is highly thermodynamically favored on the three surfaces. Particularly, the strongest interaction takes place on the (110) surface with an adsorption energy of −1.69 eV. The adsorption energy is lower on (100) and (111), −1.26 and −1.22 eV, respectively. In this context, while no significant differences are observed for the adsorption of molecular water between the three surfaces, the smaller size of the 3-fold site in the (110) surface compared to the large hollow site of the (100) facet stabilizes the *OH/*H form. Moreover, the roughness of the (111) surface prevents stabilization of the *OH/*H moieties.

Finally, we explored the possibility of water double dissociation resulting in *O and 2*H species adsorbed on the surface. As in previous cases, the lowest-energy structure involves the adsorption of each fragment in its preferred location. This implies that the three species occupy hollow sites on the (100) surface, 3-fold sites on the (110) surface, and asymmetric bridge sites on the (111) surface. In agreement with previous contributions,[22,23] these doubly dissociated structures are more stable than molecular and singly dissociated water by at least 0.3 eV. The final adsorption Gibbs energies are −1.86, −1.95, and −1.49 eV for the (100), (110), and (111) facets, respectively.

Adsorption of Two Water Molecules. The adsorption of a second water molecule is employed to assess the extent of cooperative adsorption. Initial structures for the H_2O dimer adsorptions were constructed by placing each adsorbed fragment on its preferred adsorption site. Moreover, with the aim of exploring additional structures, we also considered initial structures favoring hydrogen bonding. The lowest in energy computed structures for the adsorption of two H_2O species are shown in Figures 4 and 5. The other configurations can be found in the Supporting Information Figure S5. They are classified based on the form (molecular, singly or doubly dissociated) of water molecules, herein referred to as "mol/mol" (Figure 4a), "mol/dis" (Figure 4b), "dis/dis" (Figure 4c), "mol/2dis" (Figure 5a), "dis/2dis" (Figure 5b), and "2dis/2dis" (Figure 5c).

For mol/mol two different structures are close in energy: (i) both water molecules adsorbed at the preferred top sites with weak or no H-bonding; and (ii) one adsorbed H_2O molecule strongly interacting with the other through hydrogen bonding, with O−H···O distances of 1.70 and 1.75 Å on the (110) and

https://doi.org/10.1021/acs.jpcc.5c04170
J. Phys. Chem. C 2025, 129, 18666−18675

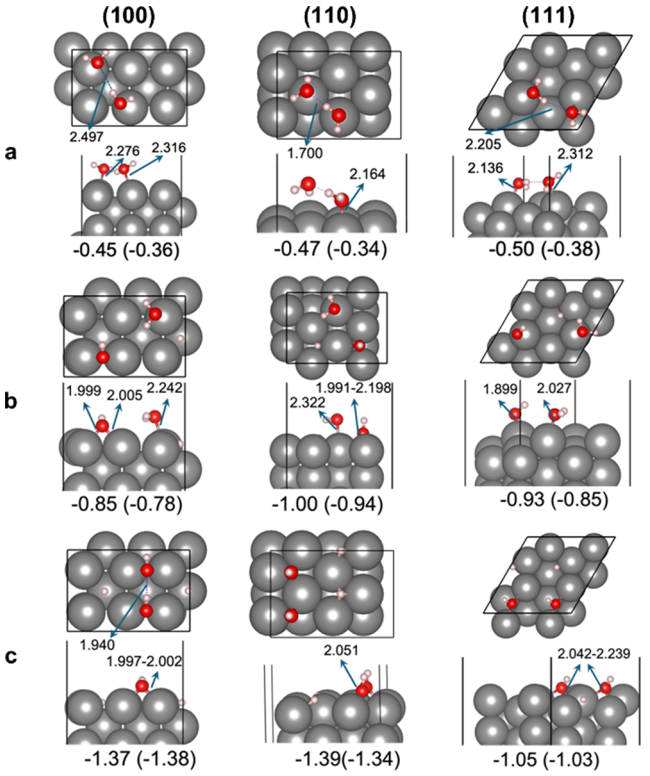

Figure 4. Optimized structures involving molecular or singly dissociated H_2O for the water dimer adsorbed on the three surfaces: (a) 2 molecular species; (b) one molecular and one dissociated species; and (c) two dissociated species. Adsorption energies (Gibbs adsorption energies) per water molecule are in eV, and O···Fe distances are in Å.

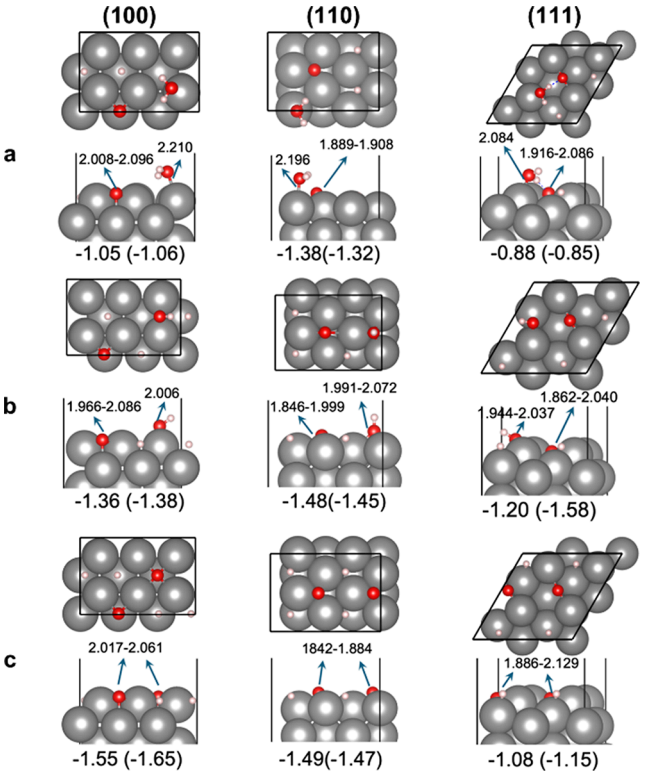

Figure 5. Optimized structures involving doubly dissociated H_2O for the water dimer adsorbed on the three surfaces. (a) one molecular and one doubly dissociated H_2O; (b) one singly dissociated and one doubly dissociated H_2O; and (c) two doubly dissociated species. Adsorption energies (Gibbs adsorption energies) per water molecule are in eV, and O···Fe distances are in Å.

(100) facets, respectively. These distances are shorter than those of the H_2O dimer at the same level of theory (1.91 Å), suggesting that the adsorbed water molecule becomes more acidic, thereby reinforcing the interaction between the two water molecules (see Bader charges for (110) surface, reported in Figure S6). When the two water molecules interact with the surface, the structure is determined by the Fe−H_2O interaction, whereas when only one H_2O molecule is adsorbed, the structure is controlled by H-bonding between both water molecules. Overall, these findings suggest that the interaction strength of H_2O with iron surfaces is similar to the interaction strength between water molecules themselves, and thus, the most stable configuration depends on the combination of multiple factors. Moreover, the adsorption energy per water molecule is essentially equal to that of the adsorption of an isolated water molecule.

The most stable computed structures among configurations involving at least one singly dissociated H_2O result from having each adsorbed fragment in its preferred site. This implies that H_2O molecules are on top sites, and *OH, *O, and *H are located on more coordinated sites. On the (100) surface, the *OH adsorbs on bridge sites, while *O and *H occupy hollow sites; on the (110) facet, the *OH, *O and *H are always in 3-fold sites; and finally, on the (111) surface, the *OH, *O, and *H species prefer all asymmetric bridge sites. Moreover, the adsorbed moieties (*H_2O, *OH, *O, and *H) are usually far apart, exhibiting little to no hydrogen bonding between them. The only exceptions are the structures including one molecular H_2O on the (111) facet, where the *OH···O distance is small. The computed distance is 1.44 Å in the mol/dis structure and 1.71 Å in the mol/2dis configuration. Consequently, the Gibbs adsorption energies per water in all configurations presenting at least one dissociated H_2O configuration tend to be close, but usually lower than the average adsorption energies of the individual H_2O in each specific form. Remarkably, the decrease is more pronounced for the configurations presenting *O species. This is very likely because doubly dissociated H_2O requires three adsorption sites, and the presence of a larger number of adsorbates makes the charge transfer from *OH, *O, and *H groups less efficient (see the Bader charges for dissociated adsorbed molecules in the (110) facet in Figures S4 and S6). Finally, for the structures containing molecular water on the (111) structure, the adsorption energy per water molecule tends to be equal to or higher than the average value due to the presence of the H-bond between the H_2O and the *OH or *O moieties. Noteworthily, these motifs play an important role in other hydrated surfaces as well.[41,42]

Remarkably, since the adsorption Gibbs energy increases significantly with the degree of water dissociation, the three facets favor dissociation. For the adsorption of an isolated water molecule, the strongest interaction on the three surfaces is associated with the doubly dissociated configuration, and the weakest one is related to the molecular form. However, the presence of two doubly dissociated water molecules implies a larger decrease in the adsorption energy per water molecule than in the other cases. Therefore, the difference between Gibbs adsorption energies per water molecule between the six potential dimer configurations becomes smaller than the Gibbs

https://doi.org/10.1021/acs.jpcc.5c04170
J. Phys. Chem. C 2025, 129, 18666−18675

energy differences found for the adsorption of a single H_2O. The preferred adsorption structure of the water dimer is 2dis/2dis on the (100) surface, and dis/2dis on the (111) and (110) surfaces, with both 2dis/2dis and dis/2dis presenting very similar energies.

Overall, the three facets favor the presence of one or two *O over molecular water, while the Gibbs adsorption energy per water molecule and the preference for dissociation decrease with increasing surface coverage.

Adsorption of a Water Monolayer. Regardless of the number of directly adsorbed molecules in each case, we defined the water monolayer as one water molecule for the Fe center in the outermost surface layer. Accordingly, we included 6 H_2O, 8 H_2O, and 4 H_2O molecules to model the monolayer on the (100), (110), and (111) surfaces, respectively. For the (111) surface, we also considered 8 water molecules due to the large separation between the external Fe sites, as single H_2O adsorption involves several outermost layers. Initially, we examined 0%, 50%, and 100% water dissociation degrees for each surface. Moreover, for (110), which presents a larger number of adsorption sites, we also considered 25% and 75% water dissociation ratios. We considered several initial structures for each degree of dissociation. These structures were constructed by considering the most stable configuration for each individual adsorbed dimer and the formation of hydrogen bonding that could stabilize the overall structure. However, some randomly distributed structures were also used to explore less common situations. Although other more stable structures could exist, the energy differences found across the explored structures make us confident that the Gibbs adsorption energies per water molecule and the final degree of dissociation are well described with our methodology.

Figure 6 shows the lowest energy computed structures on each surface as well as the degree of dissociation. Other

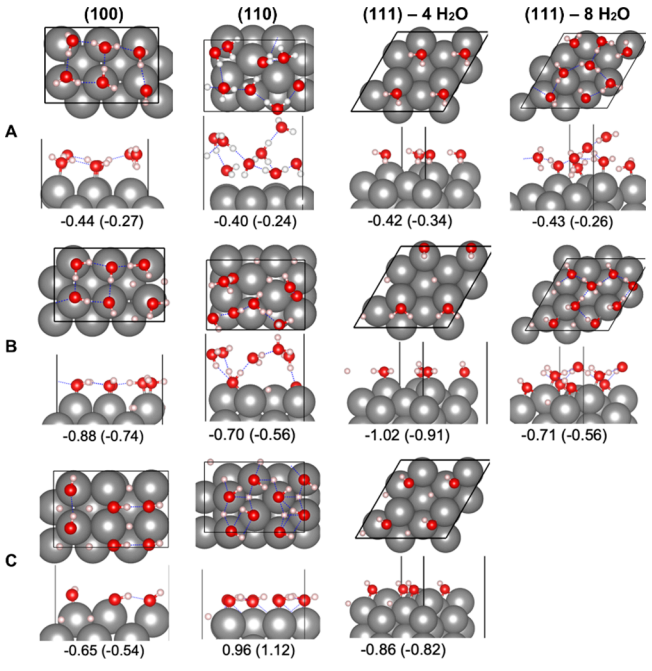

Figure 6. Optimized structures for water monolayer on the three surfaces: (A) 0% dissociation; (B) partial dissociation; and (C) complete dissociation. Adsorption energies (Gibbs adsorption energies) per water molecule are in eV.

computed structures can be found in the Supporting Information (Figures S7–S9). As noted above, the Fe–H_2O interaction competes with hydrogen bonding between adsorbed and nonadsorbed water molecules; thus, the resulting structures for 0% dissociation show only 3 (out of 6), 2 and 4 (out of 8) adsorbed molecules for the (100), (110), and (111) surfaces, respectively. In all cases, adsorbed molecules are on top sites and interact through H-bonding with the other water molecules located in a second layer. The adsorption energy per water molecule ranges between −0.40 and −0.44 eV, similar to those found for lower coverages. This confirms the similar strength of the Fe–H_2O and H-bond interactions between water molecules.

The lowest energy structures found for the adsorption of the fully dissociated water monolayer on the three facets present all of the dissociated *OH and *H groups chemisorbed on the surface (Figure 6c). For (100), the *H adsorbates are all in hollow sites, and the distribution of *OH is as follows: four *OH adsorbates are located on the most stable bridge sites. This triggers the distortion of the outermost Fe layer to accommodate both the *OH on bridges and the *H in hollow sites, while the other two *OH do not fit in the remaining bridge sites and thus they accommodate on top. For (110), the *H groups are all in the most stable 3-fold centers. In contrast, the *OH are all in the less stable top site. This is again the result of steric crowding stemming from the large number of adsorbed species (8OH/8H), which prevents the optimal distribution of the adsorbates. Finally, for the less crowded water monolayer on the (111) surface, the four *OH and *H groups are in the most stable asymmetric bridge sites. The adsorption energy per water molecule ranges between −0.86 and +0.96 eV. These values are smaller than those obtained for an isolated dissociated water molecule, and this decrease is the result of the competition for the most favorable location of each fragment and the fact that the number of groups interacting with the surface Fe increases. Note that, for the case of the (110) facet, where 8 water molecules are considered, the adsorption of dissociated water becomes thermodynamically unfavorable (+0.96 eV).

Finally, we analyze the structures presenting partial water dissociation. In all cases, except for the 25 and 50% of water dissociation on the (110), water molecules adsorb on Fe top sites, and they interact through hydrogen bonding among themselves and with the surface *OH groups. In the case of the 25% and 50% water dissociation on the (110) facet, most of the H_2O molecules are not adsorbed. Moreover, in all considered structures, the *O and *H atoms from the dissociated species consistently occupy their preferred adsorption site (hollow, 3-fold, and asymmetric bridge for (100), (110), and (111), respectively). Finally, the position of *OH is highly dependent on both the degree of water dissociation and the surface facet. For (100) and 50% of water dissociation, all *OH groups are located on a top site. For (110) and 25% water dissociation, the *OH groups occupy the most stable 3-fold sites. Finally, for 75% of water dissociation on (110) again, the *OH species are all on top. Regarding the presence of *O in the final structures, the most stable structure found for the 50% water dissociation on the (110) surface presents 5 molecular H_2O, two *OH/*H dissociated pairs, and 1 double dissociated (*O/2*H) species. However, for the other facets and degrees of dissociation, structures with 1 doubly dissociated H_2O are slightly less stable than configurations with the same number of *H species but

https://doi.org/10.1021/acs.jpcc.5c04170
J. Phys. Chem. C 2025, 129, 18666–18675

presenting only *OH/*H groups. Finally, for the (111) surface, the *OH and H_2O adsorbates are all on top to maximize the hydrogen bonding between adsorbed species.

Overall, the water adsorption energy per molecule of the most stable structures with partial dissociation on the three surfaces ranges between −0.70 and −1.02 eV. These values are higher than those computed for the fully molecular or fully dissociated monolayers, and they are similar to those obtained for the adsorption of one molecular and one dissociated isolated water species. Remarkably, for (100) and (110), the adsorption tends to weaken due to the large number of occupied sites, while it increases for (111), where a very efficient hydrogen bond network between adsorbed species is established.

Overall, water dissociation on Fe surfaces requires at least two adsorption sites involving more than one metal center. Therefore, increasing water coverage makes water dissociation less favorable, and this decreases the average adsorption energy per molecule. This effect is even more pronounced for the doubly dissociated H_2O, which is not present in the most stable computed structures, except for the 50% dissociation on the (110) surface. The adsorption of molecular H_2O is less affected by the increase of water coverage because the hydrogen bonding involving nonadsorbed species is of similar strength as the Fe−H_2O interaction. Consequently, the configuration for which only a few dissociated water molecules are adsorbed and the rest of the monolayer interacts through hydrogen bonding becomes the most favorable one, with the final degree of dissociation depending on the subtle balance between all interactions, yet always close to 50%.

Surface Termination as a Function of the Applied Potential and pH. Once we defined the preferred structure for the water monolayer, we decided to explore how surface termination is influenced by the applied potential. For that, we assumed Nørskov's computational hydrogen electrode and modeling PCETs through sequential addition (conversely, removal) of a half layer of H^+ and e^- to the surface. That is, for the (100) we added/removed 3 H^+ and 3 e^- in each step, while for the (110) and (111) surfaces we added/removed 4 H^+ and 4 e^- in each step. For each termination, we explored a variety of configurations that were constructed by adding/removing the H atoms from either the surface or the adsorbed ligands. The most relevant structures are reported in the Supporting Information (Figures S10−S12).

The addition of the first half monolayer of H^+ and e^- on the three surfaces follows different patterns. For (100), three sequential PCETs to the most stable structure of the water monolayer imply the addition of 3 *H in the empty hollows without affecting the global number of *OH/H_2O species in the final structure. In contrast, in the case of the (110) surface, the addition of 4H^+ and 4e^- implies the protonation of the two *OH groups and the double protonation of *O without increasing the number of hydrides (4) at the surface. Finally, the behavior of the (111) surface is in between the other two; 2 (of the 4) added H^+ and e^- are added on the surface, and the other 2 form 2 H_2O molecules with the adsorbed *OH groups. This is likely a consequence of the number of empty hollow, 3-fold, or asymmetric bridge sites in the different surfaces: (i) the water monolayer on the (100) surface still presents 3 unoccupied hollow sites; (ii) the water monolayer on the (111) surface presents no additional asymmetric bridge sites; and (iii) (110) has still available 3-fold sites that are strongly coupled to the sites occupied by the *OH groups. Regardless of the surface considered, the addition of a second set of H^+ and e^- leads to the same structure for all surfaces. This is formed by a monolayer of adsorbed *H atoms and water molecules interacting through hydrogen bonding without being directly adsorbed on the surface. For future studies, this monolayer could be modeled as a fully hydrogenated surface without explicitly adding the H_2O molecules.

Surface oxidation through proton-coupled electron-transfer steps also follows different patterns for the three surfaces. For (100), the first PCET implies the removal of adsorbed hydrides. This is followed by the removal of one H per remaining water molecule, leading to a *OH-covered surface where all *OH groups settle in their preferred bridge site. Complete oxidation implies the formation of FeO on the outermost layer with oxygen atoms occupying the hollow positions. For (111), a similar behavior to that of the (100) facet is observed. That is, the desorbed H originates sequentially from adsorbed H, then from water molecules at the electrolyte−electrode interface, and finally from adsorbed *OH. The only exception is the *OH-covered surface, which is less stable than a configuration with 2 H_2O, 4 *OH, and 2 *O. For (110), the pattern is more complex, mainly due to the high stabilization of O atoms on the surface, even for nonoxidized terminations. Details of the structures can be found in the Supporting Information (Figures S10−S12).

The Gibbs energies of the preferred structures within each termination are used to construct surface coverage analysis plots and Pourbaix diagrams, as described in the computational details section. Figure 7a illustrates the most stable structure as

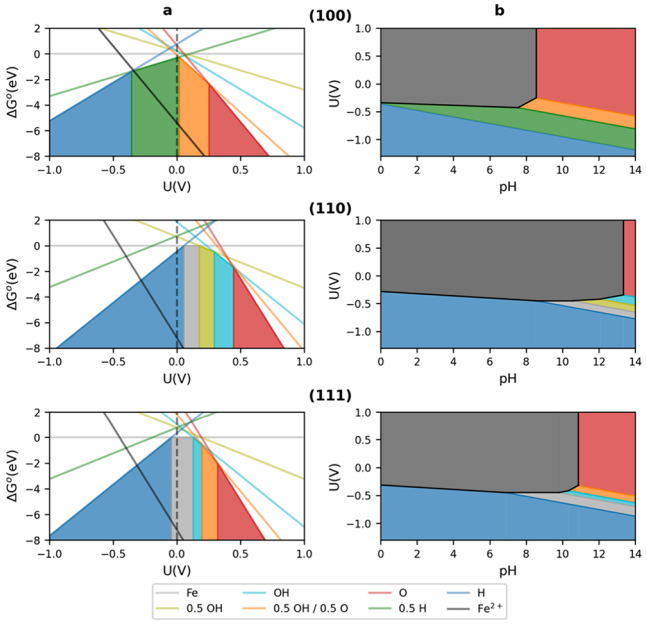

Figure 7. (a) Surface coverage analysis of Fe (100), (110), and (111) facets as a function of the potential versus RHE. (b) Pourbaix diagrams for the facets herein considered.

a function of the applied potential versus RHE, and Figure 7b shows the Pourbaix diagrams, from which we can infer the stability of each termination as a function of the pH. The dashed line in Figure 7a indicates the HER onset potential versus RHE. At pH = 0 and regardless of the considered surface, iron oxidation to Fe^{2+} is favored in the absence of any applied potential. Consequently, we focus our attention on the

https://doi.org/10.1021/acs.jpcc.5c04170
J. Phys. Chem. C 2025, 129, 18666−18675

most stable structures at reductive potentials. For the (100) facet two different structures are stable at pH = 0 and reductive conditions: (i) when the applied potential is between −0.34 and −0.36 V, the most stable structure has a half *H monolayer adsorbed and, (ii) at reductive potentials higher than −0.36 V the most stable structure shows a surface covered with *H atoms located on hollow positions. For the other two surfaces, the only stable structure at reductive conditions implies the formation of a *H monolayer on the surface. The required potential to form this structure is very similar for the two cases, the obtained values being −0.28 and −0.31 V, for the (110) and (111) facets, respectively.

Decreasing the proton concentration in the electrolyte changes the relative stability of the different terminations. First, without an applied external potential, the dissolved Fe^{2+} and FeO relative stability depends on the pH. FeO becomes the preferred structure at pH 8.56, 13.36, and 10.57 for (100), (110), and (111), respectively. In this context, Fe is easily oxidized to Fe^{2+}, in the form of either Fe^{2+} or FeO, depending on the pH of the solution and the involved surface. Indeed, this oxidation takes place even without applying an oxidative potential.

More interestingly, the structure at reductive potentials also changes with the pH of the solution. Indeed, three major structures are possible: a Fe surface covered by one *H per surface metal center (H monolayer, blue in Figure 7); a surface half covered by hydrogen atoms (H half monolayer, green in Figure 7), or a partially oxidized surface. The formation of an *H monolayer is preferred in a large variety of situations. However, its formation requires higher cathodic potentials when increasing the pH. In this context, while for the (110) and (111) surface at usual working potentials for several electrocatalytic reduction process (−0.4 to −1.0 V) the most stable structure at neutral and basic conditions is the fully hydrogenated monolayer, for the (100) facet, the most stable structure at these conditions should be an Fe surface with only half of the hollow sites occupied by H. Only in strongly alkaline environments would a clean Fe surface be more stable or, even at higher pH, partial oxidation of the surface could occur. Remarkably, iron-based materials have been reported to be active in the nitrogen reduction reaction. The best cathodic currents are commonly obtained at a neutral pH and when applying a potential of around −0.4 V. Under these conditions, our calculations suggest that Fe (100) should be either half covered by *H or half terminated with *OH and *O groups, while (110) and (111) facets should be either fully covered by *H or Fe terminated.

CONCLUSIONS

The adsorption of water on the stable low-index (100) and (110) Fe surfaces, as well as on the rough (111) facet, has been studied through DFT periodic calculations. Several molecular water coverages, from isolated water to full monolayer configurations, have been considered, as well as structures derived from the dissociated *OH/*H species. Regardless of the surface considered, the adsorption of an isolated water molecule takes place through *O/2*H doubly dissociation, which leads to partial oxidation of the outermost Fe atoms. Gibbs adsorption energies range from −1.41 to −1.95 eV, with the strongest interaction being observed for the (110) surface.

Increasing water coverage disfavors water dissociation due to the reduced availability of preferred sites on the surface. In contrast, the interaction energy per water molecule of molecular H_2O is almost unchanged when increasing H_2O coverage because the adsorption energy and the H-bonding between adsorbed and nonabsorbed molecules are similar. Consequently, the thermodynamically preferred structure for a water monolayer implies 50% H_2O dissociation and usually presents only *H_2O, *OH, and *H adsorbed species. Only in the case of the (110) surface, where water interacts strongly, the final structure is more complex, presenting even *O adsorbed species on the surface. Overall, the Gibbs adsorption energies per water molecule at full monolayer coverage are lower than for the isolated H_2O molecules and range between −0.56 and −0.91 eV, the highest values corresponding to the most efficient H-bonding network between adsorbed and nonadsorbed species.

For the herein considered facets, analysis of the surface termination as a function of the applied potential at different pH conditions suggests that Fe is easily oxidized under acidic conditions to soluble Fe^{2+} or to FeO under basic conditions, even in the absence of an applied potential. Only under very specific conditions could we obtain partially oxidized species, with said conditions being surface-dependent. Larger differences are observed when applying reductive potentials. For the (110) and (111) surfaces, the only possible reductive structure implies the formation of a H-adsorbed monolayer, which becomes the most stable structure at relatively low cathodic potentials, even in neutral (around −0.4 V) or basic environments (around −0.6 V at pH = 11). On the other hand, two reduced structures exist for the (100) surface. At moderate cathodic potentials, the most stable structure implies a surface where half of the hollow sites are occupied by adsorbed *H atoms. Raising the applied potential favors the formation of a full *H monolayer. The transition occurs when the applied potential is −0.36 V at pH = 0, and the required potential increases to −0.77 V at pH = 7 and −1.01 V at pH = 11. In this context, under usual reducing conditions, different terminations should be considered. For (110) and (111), both Fe and H-covered terminations are likely to coexist, while for (100), 0.5*OH and 0.5*H are the two most stable structures.

ASSOCIATED CONTENT

Data Availability Statement

The DFT data that support the findings of this study are available at 10.34810/data2394

Supporting Information

The Supporting Information is available free of charge at https://pubs.acs.org/doi/10.1021/acs.jpcc.5c04170.

Bader charges of one and two adsorbed water molecules on the different considered surfaces, additional, less stable structures for water adsorption at different coverages, and structures associated with the different surface terminations (PDF)

AUTHOR INFORMATION

Corresponding Authors

Luis Rodríguez-Santiago − *Departament de Química, Universitat Autònoma de Barcelona, 08193 Barcelona, Spain;* orcid.org/0000-0003-4983-4228; Email: Luis.Rodriguez.Santiago@uab.cat

Xavier Solans-Monfort − *Departament de Química, Universitat Autònoma de Barcelona, 08193 Barcelona, Spain;* orcid.org/0000-0002-2172-3895; Email: Xavier.Solans@uab.cat

Authors

Adenilson Felipe Sousa-Silva − *Departament de Química, Universitat Autònoma de Barcelona, 08193 Barcelona, Spain*

Dídac-Armand Fenoll − *Departament de Química, Universitat Autònoma de Barcelona, 08193 Barcelona, Spain;* orcid.org/0000-0003-1141-8114

Mariona Sodupe − *Departament de Química, Universitat Autònoma de Barcelona, 08193 Barcelona, Spain;* orcid.org/0000-0003-0276-0524

Complete contact information is available at: https://pubs.acs.org/10.1021/acs.jpcc.5c04170

Notes

The authors declare no competing financial interest.

■ ACKNOWLEDGMENTS

This work was supported by the grant PID2023-151738NB-I00 funded by the Spanish Ministerio de Ciencia, Innovación y Universidades (MCIU/AEI/10.13039/501100011033).

■ REFERENCES

(1) Carrasco, J.; Hodgson, A.; Michaelides, A. A Molecular Perspective of Water at Metal Interfaces. *Nat. Mater.* **2012**, *11*, 667−674.

(2) Wang, Y.-H.; Dong, J.-H.; Tan, Z.; Wang, X.-F.; Song, X.-Z. The Journey of Iron-Based Electrocatalytic Materials for Nitrogen Reduction Reaction: From Current Status to Future Prospects. *J. Mater. Chem. A Mater.* **2023**, *11*, 11048−11077.

(3) Roger, I.; Shipman, M. A.; Symes, M. D. Earth-Abundant Catalysts for Electrochemical and Photoelectrochemical Water Splitting. *Nat. Rev. Chem.* **2017**, *1*, No. 0003.

(4) Han, X.; Liu, C.; Tang, Y.; Meng, Q.; Zhou, W.; Chen, S.; Deng, S.; Wang, J. Unveiling the Role of Cobalt Doping in Optimizing Ammonia Electrosynthesis on Iron−Cobalt Oxyhydroxide Hollow Nanocages. *J. Mater. Chem. A Mater.* **2023**, *11*, 14424−14431.

(5) Zhu, X.; Liu, Z.; Wang, H.; Zhao, R.; Chen, H.; Wang, T.; Wang, F.; Luo, Y.; Wu, Y.; Sun, X. Boosting Electrocatalytic N 2 Reduction to NH 3 on β-FeOOH by Fluorine Doping. *Chem. Commun.* **2019**, *55*, 3987−3990.

(6) Hu, L.; Khaniya, A.; Wang, J.; Chen, G.; Kaden, W. E.; Feng, X. Ambient Electrochemical Ammonia Synthesis with High Selectivity on Fe/Fe Oxide Catalyst. *ACS Catal.* **2018**, *8*, 9312−9319.

(7) Kim, J. H.; Ju, H.; An, B.-S.; An, Y.; Cho, K.; Kim, S. H.; Bae, Y.-S.; Yoon, H. C. Comparison between Fe2O3/C and Fe3C/Fe2O3/Fe/C Electrocatalysts for N2 Reduction in an Alkaline Electrolyte. *ACS Appl. Mater. Interfaces* **2021**, *13*, 61316−61323.

(8) Jia, L.; Xue, H.; Xian, F.; Sugahara, Y.; Sakai, N.; Nan, J.; Yamauchi, Y.; Sasaki, T.; Ma, R. Porous and Partially Dehydrogenated Fe2+-Containing Iron Oxyhydroxide Nanosheets for Efficient Electrochemical Nitrogen Reduction Reaction (ENRR). *Small* **2023**, *19*, No. 2303221.

(9) Zhao, M.; Wang, J.; Wang, X.; Xu, J.; Liu, L.; Yang, W.; Feng, J.; Song, S.; Zhang, H. Creating Highly Active Iron Sites in Electrochemical N2 Reduction by Fabricating Strongly-Coupled Interfaces. *Small* **2023**, *19*, No. 2205313.

(10) Seh, Z. W.; Kibsgaard, J.; Dickens, C. F.; Chorkendorff, I.; Nørskov, J. K.; Jaramillo, T. F. Combining Theory and Experiment in Electrocatalysis: Insights into Materials Design. *Science* **2017**, *355*, No. eaad4998.

(11) Guo, W.; Zhang, K.; Liang, Z.; Zou, R.; Xu, Q. Electrochemical Nitrogen Fixation and Utilization: Theories, Advanced Catalyst Materials and System Design. *Chem. Soc. Rev.* **2019**, *48*, 5658−5716.

(12) Liu, W.; Sun, J.; Ye, C. The Influence of Tensile Strain on Water Adsorbed on Fe (100) Surface: Surface Chemistry Aspect of Stress Corrosion Cracking. *Appl. Surf. Sci.* **2019**, *481*, 192−199.

(13) Müssig, H.-J.; Arabczyk, W. Water Vapour Adsorption on the Iron(111) Surface Studied by LEED and WFC. *Kristall und Technik* **1981**, *16*, 827−835.

(14) Dwyer, D. J.; Simmons, G. W.; Wei, R. P. A Study of the Initial Reaction of Water Vapor with Fe(001) Surface. *Surf. Sci.* **1977**, *64*, 617−632.

(15) Baró, A. M.; Erley, W. The Adsorption of H $_2$ O on Fe(100) Studied by EELS. *J. Vac. Sci. Technol.* **1982**, *20*, 580−583.

(16) Liu, S.; Tian, X.; Wang, T.; Wen, X.; Li, Y. W.; Wang, J.; Jiao, H. High Coverage Water Aggregation and Dissociation on Fe(100): A Computational Analysis. *J. Phys. Chem. C* **2014**, *118*, 26139−26154.

(17) Freitas, R. R. Q.; Rivelino, R.; Mota, F. D. B.; de Castilho, C. M. C. Dissociative Adsorption and Aggregation of Water on the Fe(100) Surface: A DFT Study. *J. Phys. Chem. C* **2012**, *116*, 20306−20314.

(18) Lazar, P.; Otyepka, M. Dissociation of Water at Iron Surfaces: Generalized Gradient Functional and Range-Separated Hybrid Functional Study. *J. Phys. Chem. C* **2012**, *116*, 25470−25477.

(19) White, J. J.; Hinsch, J. J.; Bennett, W. W.; Wang, Y. Theoretical Understanding of Water Adsorption on Stepped Iron Surfaces. *Appl. Surf. Sci.* **2022**, *605*, No. 154650.

(20) Ossowski, T.; Silva, J. L. F., Da; Kiejna, A. Water Adsorption on the Stoichiometric and Defected Fe(110) Surfaces. *Surf. Sci.* **2018**, *668*, 144−149.

(21) Wang, W.; Wang, G.; Shao, M. First-Principles Modeling of Direct versus Oxygen-Assisted Water Dissociation on Fe(100) Surfaces. *Catalysts* **2016**, *6*, 29.

(22) Liu, S.; Tian, X.; Wang, T.; Wen, X.; Li, Y.-W.; Wang, J.; Jiao, H. Coverage Dependent Water Dissociative Adsorption on Fe (110) from DFT Computation. *Phys. Chem. Chem. Phys.* **2015**, *17*, 8811−8821.

(23) Liu, S.; Tian, X.; Wang, T.; Wen, X.; Li, Y.-W.; Wang, J.; Jiao, H. Coverage Dependent Water Dissociative Adsorption on the Clean and O-Precovered Fe(111) Surfaces. *J. Phys. Chem. C* **2015**, *119*, 11714−11724.

(24) Kavalsky, L.; Viswanathan, V. Electrowinning for Room-Temperature Ironmaking: Mapping the Electrochemical Aqueous Iron Interface. *J. Phys. Chem. C* **2024**, *128*, 14611−14620.

(25) Kresse, G.; Hafner, J. Ab Initio Molecular Dynamics for Liquid Metals. *Phys. Rev. B* **1993**, *47*, 558−561.

(26) Kresse, G.; Furthmüller, J. Efficient Iterative Schemes for Ab Initio Total-Energy Calculations Using a Plane-Wave Basis Set. *Phys. Rev. B* **1996**, *54*, 11169−11186.

(27) Hjorth Larsen, A.; Jørgen Mortensen, J.; Blomqvist, J.; Castelli, I. E.; Christensen, R.; Dułak, M.; Friis, J.; Groves, M. N.; Hammer, B.; Hargus, C.; et al. The Atomic Simulation Environment—a Python Library for Working with Atoms. *J. Phys.: Condens. Matter* **2017**, *29*, 273002.

(28) Perdew, J. P.; Burke, K.; Ernzerhof, M. Generalized Gradient Approximation Made Simple. *Phys. Rev. Lett.* **1996**, *77*, 3865−3868.

(29) Grimme, S.; Antony, J.; Ehrlich, S.; Krieg, H. A Consistent and Accurate Ab Initio Parametrization of Density Functional Dispersion Correction (DFT-D) for the 94 Elements H-Pu. *J. Chem. Phys.* **2010**, *132*, 154104.

(30) Blöchl, P. E. Projector Augmented-Wave Method. *Phys. Rev. B* **1994**, *50*, 17953.

(31) Kresse, G.; Joubert, D. From Ultrasoft Pseudopotentials to the Projector Augmented-Wave Method. *Phys. Rev. B* **1999**, *59*, 1758−1775.

(32) Mathew, K.; Sundararaman, R.; Letchworth-Weaver, K.; Arias, T. A.; Hennig, R. G. Implicit Solvation Model for Density-Functional Study of Nanocrystal Surfaces and Reaction Pathways. *J. Chem. Phys.* **2014**, *140*, No. 084106.

(33) Henkelman, G.; Arnaldsson, A.; Jónsson, H. A Fast and Robust Algorithm for Bader Decomposition of Charge Density. *Comput. Mater. Sci.* **2006**, *36*, 354−360.

(34) Bader, R. F. W. A Quantum Theory of Molecular Structure and Its Applications. *Chem. Rev.* **1991**, *91*, 893−928.

(35) Nørskov, J. K.; Rossmeisl, J.; Logadottir, A.; Lindqvist, L.; Kitchin, J. R.; Bligaard, T.; Jónsson, H. Origin of the Overpotential for Oxygen Reduction at a Fuel-Cell Cathode. *J. Phys. Chem. B* **2004**, *108*, 17886−17892.
(36) Wang, V.; Xu, N.; Liu, J.-C.; Tang, G.; Geng, W.-T. VASPKIT: A User-Friendly Interface Facilitating High-Throughput Computing and Analysis Using VASP Code. *Comput. Phys. Commun.* **2021**, *267*, No. 108033.
(37) González, D.; Sodupe, M.; Rodríguez-Santiago, L.; Solans-Monfort, X. Surface Morphology Controls Water Dissociation on Hydrated IrO 2 Nanoparticles. *Nanoscale* **2021**, *13*, 14480−14489.
(38) González, D.; Sodupe, M.; Rodríguez-Santiago, L.; Solans-Monfort, X. Metal Coordination Determines the Catalytic Activity of IrO2 Nanoparticles for the Oxygen Evolution Reaction. *J. Catal.* **2022**, *412*, 78−86.
(39) González, D.; Heras-Domingo, J.; Sodupe, M.; Rodríguez-Santiago, L.; Solans-Monfort, X. Importance of the Oxyl Character on the IrO2 Surface Dependent Catalytic Activity for the Oxygen Evolution Reaction. *J. Catal.* **2021**, *396*, 192−201.
(40) Bratsch, S. G. Standard Electrode Potentials and Temperature Coefficients in Water at 298.15 K. *J. Phys. Chem. Ref. Data* **1989**, *18*, 1−21.
(41) Heras-Domingo, J.; Sodupe, M.; Solans-Monfort, X. Interaction between Ruthenium Oxide Surfaces and Water Molecules. Effect of Surface Morphology and Water Coverage. *J. Phys. Chem. C* **2019**, *123*, 7786−7798.
(42) González, D.; Heras-Domingo, J.; Pantaleone, S.; Rimola, A.; Rodríguez-Santiago, L.; Solans-Monfort, X.; Sodupe, M. Water Adsorption on MO_2 (M = Ti, Ru, and Ir) Surfaces. Importance of Octahedral Distortion and Cooperative Effects. *ACS Omega* **2019**, *4*, 2989−2999.

https://doi.org/10.1021/acs.jpcc.5c04170
J. Phys. Chem. C 2025, 129, 18666−18675